Draft version June 15, 2022
Typeset using LaTeX **twocolumn** style in AASTeX631

arXiv:2206.06713v1 [astro-ph.HE] 14 Jun 2022

X-ray polarization detection of Cassiopeia A with IXPE

Jacco Vink,[1] Dmitry Prokhorov,[1] Riccardo Ferrazzoli,[2] Patrick Slane,[3] Ping Zhou,[4] Kazunori Asakura,[5] Luca Baldini,[6,7] Niccolò Bucciantini,[8,9,10] Enrico Costa,[2] Alessandro Di Marco,[2] Jeremy Heyl,[11] Frédéric Marin,[12] Tsunefumi Mizuno,[13] C.-Y. Ng,[14] Melissa Pesce-Rollins,[6] Brian D. Ramsey,[15] John Rankin,[2] Ajay Ratheesh,[2] Carmelo Sgrò,[6] Paolo Soffitta,[2] Douglas A. Swartz,[15] Toru Tamagawa,[16] Martin C. Weisskopf,[15] Yi-Jung Yang,[14,17] Ronaldo Bellazzini,[6] Raffaella Bonino,[18,19] Elisabetta Cavazzuti,[20] Luigi Costamante,[20] Niccolò Di Lalla,[21] Luca Latronico,[18] Simone Maldera,[18] Alberto Manfreda,[6] Francesco Massaro,[18,19] Ikuyuki Mitsuishi,[22] Nicola Omodei,[21] Chiara Oppedisano,[18] Silvia Zane,[23] Ivan Agudo,[24] Lucio A. Antonelli,[25,26] Matteo Bachetti,[27] Wayne H. Baumgartner,[15] Stefano Bianchi,[28] Stephen D. Bongiorno,[15] Alessandro Brez,[6] Fiamma Capitanio,[2] Simone Castellano,[6] Stefano Ciprini,[29,26] Alessandra De Rosa,[2] Ettore Del Monte,[2] Laura Di Gesu,[20] Immacolata Donnarumma,[20] Victor Doroshenko,[30,31] Michal Dovčiak,[32] Steven R. Ehlert,[15] Teruaki Enoto,[16] Yuri Evangelista,[2] Sergio Fabiani,[2] Javier A. Garcia,[33] Shuichi Gunji,[34] Kiyoshi Hayashida,[35] Wataru Iwakiri,[36] Svetlana G. Jorstad,[37,38] Vladimir Karas,[32] Takao Kitaguchi,[16] Jeffery J. Kolodziejczak,[15] Henric Krawczynski,[39] Fabio La Monaca,[2] Ioannis Liodakis,[40] Andrea Marinucci,[20] Alan P. Marscher,[37] Herman L. Marshall,[41] Giorgio Matt,[28] Fabio Muleri,[2] Stephen L. O'Dell,[15] Alessandro Papitto,[25] George G. Pavlov,[42] Abel L. Peirson,[21] Matteo Perri,[26,25] Pierre-Olivier Petrucci,[43] Maura Pilia,[27] Andrea Possenti,[27] Juri Poutanen,[44,31] Simonetta Puccetti,[26] Roger W. Romani,[21] Gloria Spandre,[6] Fabrizio Tavecchio,[45] Roberto Taverna,[46] Yuzuru Tawara,[22] Allyn F. Tennant,[15] Nicolas E. Thomas,[15] Francesco Tombesi,[47,29,48] Alessio Trois,[27] Sergey Tsygankov,[44,31] Roberto Turolla,[46,23] Kinwah Wu,[23] and Fei Xie[49]

[1] *Anton Pannekoek Institute for Astronomy & GRAPPA, University of Amsterdam, Science Park 904, 1098 XH Amsterdam, The Netherlands*
[2] *INAF Istituto di Astrofisica e Planetologia Spaziali, Via del Fosso del Cavaliere 100, 00133 Roma, Italy*
[3] *Center for Astrophysics, Harvard & Smithsonian, 60 Garden St, Cambridge, MA 02138, USA*
[4] *School of Astronomy and Space Science, Nanjing University, Nanjing 210023, PR China*
[5] *Osaka University, Graduate School of Science, Osaka, Japan*
[6] *Istituto Nazionale di Fisica Nucleare, Sezione di Pisa, Largo B. Pontecorvo 3, 56127 Pisa, Italy*
[7] *Dipartimento di Fisica, Università di Pisa, Largo B. Pontecorvo 3, 56127 Pisa, Italy*
[8] *INAF Osservatorio Astrofisico di Arcetri, Largo Enrico Fermi 5, 50125 Firenze, Italy*
[9] *Dipartimento di Fisica e Astronomia, Università degli Studi di Firenze, Via Sansone 1, 50019 Sesto Fiorentino (FI), Italy*
[10] *Istituto Nazionale di Fisica Nucleare, Sezione di Firenze, Via Sansone 1, 50019 Sesto Fiorentino (FI), Italy*
[11] *University of British Columbia, Vancouver, BC V6T 1Z4, Canada*
[12] *Université de Strasbourg, CNRS, Observatoire Astronomique de Strasbourg, UMR 7550, 67000 Strasbourg, France*
[13] *Hiroshima Astrophysical Science Center, Hiroshima University, 1-3-1 Kagamiyama, Higashi-Hiroshima, Hiroshima 739-8526, Japan*
[14] *Department of Physics, The University of Hong Kong, Pokfulam, Hong Kong*
[15] *NASA Marshall Space Flight Center, Huntsville, AL 35812, USA*
[16] *RIKEN Cluster for Pioneering Research, 2-1 Hirosawa, Wako, Saitama 351-0198, Japan*
[17] *Laboratory for Space Research, The University of Hong Kong, Hong Kong*
[18] *Istituto Nazionale di Fisica Nucleare, Sezione di Torino, Via Pietro Giuria 1, 10125 Torino, Italy*
[19] *Dipartimento di Fisica, Università degli Studi di Torino, Via Pietro Giuria 1, 10125 Torino, Italy*
[20] *ASI - Agenzia Spaziale Italiana, Via del Politecnico snc, 00133 Roma, Italy*
[21] *Department of Physics and Kavli Institute for Particle Astrophysics and Cosmology, Stanford University, Stanford, California 94305, USA*
[22] *Graduate School of Science, Division of Particle and Astrophysical Science, Nagoya University, Furo-cho, Chikusa-ku, Nagoya, Aichi 464-8602, Japan*
[23] *Mullard Space Science Laboratory, University College London, Holmbury St Mary, Dorking, Surrey RH5 6NT, UK*
[24] *Instituto de Astrofísicade Andalucía, IAA-CSIC, Glorieta de la Astronomía s/n, 18008 Granada, Spain*
[25] *INAF Osservatorio Astronomico di Roma, Via Frascati 33, 00078 Monte Porzio Catone (RM), Italy*
[26] *Space Science Data Center, Agenzia Spaziale Italiana, Via del Politecnico snc, 00133 Roma, Italy*

Corresponding author: Jacco Vink
j.vink@uva.nl

[27]INAF Osservatorio Astronomico di Cagliari, Via della Scienza 5, 09047 Selargius (CA), Italy
[28]Dipartimento di Matematica e Fisica, Università degli Studi Roma Tre, Via della Vasca Navale 84, 00146 Roma, Italy
[29]Istituto Nazionale di Fisica Nucleare, Sezione di Roma "Tor Vergata", Via della Ricerca Scientifica 1, 00133 Roma, Italy
[30]Institut für Astronomie und Astrophysik, Universität Tübingen, Sand 1, 72076 Tübingen, Germany
[31]Space Research Institute of the Russian Academy of Sciences, Profsoyuznaya Str. 84/32, Moscow 117997, Russia
[32]Astronomical Institute of the Czech Academy of Sciences, Boční II 1401/1, 14100 Praha 4, Czech Republic
[33]California Institute of Technology, Pasadena, CA 91125, USA
[34]Yamagata University,1-4-12 Kojirakawa-machi, Yamagata-shi 990-8560, Japan
[35]Osaka University, 1-1 Yamadaoka, Suita, Osaka 565-0871, Japan
[36]Department of Physics, Faculty of Science and Engineering, Chuo University, 1-13-27 Kasuga, Bunkyo-ku, Tokyo 112-8551, Japan
[37]Institute for Astrophysical Research, Boston University, 725 Commonwealth Avenue, Boston, MA 02215, USA
[38]Department of Astrophysics, St. Petersburg State University, Universitetsky pr. 28, Petrodvoretz, 198504 St. Petersburg, Russia
[39]Physics Department and McDonnell Center for the Space Sciences, Washington University in St. Louis, St. Louis, MO 63130, USA
[40]Finnish Centre for Astronomy with ESO, 20014 University of Turku, Finland
[41]MIT Kavli Institute for Astrophysics and Space Research, Massachusetts Institute of Technology, 77 Massachusetts Avenue, Cambridge, MA 02139, USA
[42]Department of Astronomy and Astrophysics, Pennsylvania State University, University Park, PA 16802, USA
[43]Université Grenoble Alpes, CNRS, IPAG, 38000 Grenoble, France
[44]Department of Physics and Astronomy, 20014 University of Turku, Finland
[45]INAF Osservatorio Astronomico di Brera, Via E. Bianchi 46, 23807 Merate (LC), Italy
[46]Dipartimento di Fisica e Astronomia, Università degli Studi di Padova, Via Marzolo 8, 35131 Padova, Italy
[47]Dipartimento di Fisica, Università degli Studi di Roma "Tor Vergata", Via della Ricerca Scientifica 1, 00133 Roma, Italy
[48]Department of Astronomy, University of Maryland, College Park, Maryland 20742, USA
[49]Guangxi Key Laboratory for Relativistic Astrophysics, School of Physical Science and Technology, Guangxi University, Nanning 530004, China

ABSTRACT

We report on a $\sim 5\sigma$ detection of polarized 3–6 keV X-ray emission from the supernova remnant Cassiopeia A with the Imaging X-ray Polarimetry Explorer (IXPE) mission. The overall polarization degree of $1.8 \pm 0.3\%$ is detected by summing over a large region assuming circular symmetry for the polarization vectors. Correcting for thermal X-ray emission implies a $\sim 2.4\%$ polarization degree for the synchrotron component. For the X-ray synchrotron dominated forward shock region the polarization degree of the synchrotron component is close to 5%. A pixel-by-pixel search for polarization provides a few tentative detections from discrete regions at the $\sim 3\sigma$ confidence level. Given the number of pixels, the significance is insufficient to claim a detection for individual pixels, but implies considerable turbulence on small scales. Cas A's X-ray continuum emission is dominated by synchrotron radiation from regions within $\lesssim 10^{17}$ cm of the forward- and reverse shocks. We find that i) the measured polarization angle corresponds to a radially-oriented magnetic field similar to what has been inferred from radio observations; ii) the X-ray polarization degree is lower than in the radio band ($\sim 5\%$). Since shock compression should impose a tangential magnetic field structure, the IXPE results imply that magnetic-fields are reoriented within $\sim 10^{17}$ cm of the shock. If the magnetic-field alignment is due to locally enhanced acceleration near quasi-parallel shocks, the preferred X-ray polarization angle suggests a size of 3×10^{16} cm for cells with radial magnetic fields.

Keywords: Polarimetry (1278) — Supernova remnants (1667) — X-ray astronomy (1810) — Shocks (2086)

1. INTRODUCTION

Supernova remnants (SNRs) have long been known to be sources of radio synchrotron radiation (Shklovsky 1954), emitted by relativistic electrons, which are now recognized to be accelerated through the diffusive shock acceleration (DSA) process (e.g., Malkov & Drury 2001). According to DSA theory, energetic, charged particles move diffusively through the plasma—due to scattering on magnetic-field fluctuations—and gain energy by repeatedly crossing the shock front, with each shock crossing providing a few percent gain in momentum. The presence of relativistic electrons has been key for identifying SNR shocks—as opposed to the supernova explosions themselves— as locations for Galactic cosmic-ray acceleration. Although the link between cosmic rays and SNRs has also been confirmed by gamma-ray detections of many SNRs (e.g. Helder et al. 2012; Funk 2017, for reviews), important information about the cosmic-ray acceleration process and shock conditions has been obtained from the detection and characterisation of X-ray synchrotron emission from young SNRs, starting with the discovery of X-ray synchrotron radiation from the rims of SN 1006 (Koyama et al. 1995).

The $\sim$10–100 TeV electrons responsible for the X-ray synchrotron radiation have radiative-loss timescales that are short compared to the SNR ages: $\tau_{\rm loss} \approx 12.5 E_{14}^{-2} B_{-4}^{-1}$ yr, with E_{14} the electron energy in units of 100 TeV and $B_{-4} \equiv B/10^{-4}$ G. X-ray synchrotron radiation from SNRs, therefore, indicates that the 10–100 TeV electrons have been accelerated recently and on short time scales. According to DSA theory, reaching such high energies requires highly turbulent fields — $|\delta B/B| \sim 1$ — resulting in mean-free-path lengths of the order of the gyroradius for these electrons.

Synchrotron radiation is intrinsically polarized at the $\sim$ 70% level (Ginzburg & Syrovatskii 1965), with the polarization angle informing us about the local magnetic-field orientation, and the polarization degree being dependent on the uniformity of the magnetic-field orientation along the line of sight of observed regions. Mature SNRs ($\gtrsim$ 2000 yr) tend to have magnetic fields that are tangentially oriented with respect to the radial direction, whereas young SNRs have radially oriented magnetic fields (Dickel & Milne 1976). The polarization degree in the radio band is also different between young and mature SNRs, with mature SNRs generally having polarization degrees above 10%, while young SNRs ($\lesssim$ 2000 yr) generally have polarization degrees below 10% (Dickel & Jones 1990; Sun et al. 2011). The radial orientation of the magnetic fields in young SNRs is not well understood from a theoretical point of view, but see Zirakashvili & Ptuskin (2008); Inoue et al. (2013); West et al. (2017) for a number of hypotheses. It is not known whether the radially oriented field is immediately established at the shock front. It may well be that the fields closer to the shock fronts are tangentially oriented (Jun & Norman 1996; Bykov et al. 2020), since the shock compresses, and thus enhances, the tangential component of the pre-shock magnetic field.

An object that has in many ways been central to the discussion of radio and X-ray synchrotron radiation from SNRs is the young ($\sim$ 350 yr) and bright core-collapse SNR Cassiopeia A (Cas A), located at a distance of 3.4 kpc (Reed et al. 1995). Cas A has a radially oriented magnetic-field (e.g. Rosenberg 1970; Braun et al. 1987), and a polarization degree in the radio band of only 5% in the bright shell, and 8–10% in the outer regions (e.g. Anderson et al. 1995). The $\sim$ 5% level of polarization degree has been established at radio frequencies from 20–100 GHz (Mayer & Hollinger 1968; Flett & Henderson 1979; Kenney & Dent 1985) and even in the infrared, at 2.2 μm, for a segment in the northwest of Cas A (Jones et al. 2003). At these high frequencies Faraday rotation is negligible—see also (Kenney & Dent 1985)—and the only factor contributing to the low polarization degree is the non-uniformity of the magnetic-field directions within a angular resolution element and integrated along the line of sight.

X-ray polarization measurements are in that respect highly interesting. First of all, the rapid radiative losses of the 10–100 TeV electrons mean that X-ray synchrotron emission originates from plasma that is confined to thin regions downstream of the shock, with a typical width of $l_{\rm loss} \approx \Delta v \tau_{\rm loss}$, with $\Delta v = \frac{1}{4} V_{\rm sh}$. For Cas A the shock velocity is $V_{\rm sh} \approx 5000$–$6000\ {\rm km\,s^{-1}}$ (e.g Patnaude & Fesen 2009; Vink et al. 2022). Indeed, the observed widths of the X-ray synchrotron filaments of $1''$–$2''$ ($l \approx 10^{17}$ cm) suggests that the local, downstream magnetic-field strengths are $B \approx 250$–$550\ \mu$G (Vink & Laming 2003; Bamba et al. 2005; Völk et al. 2005; Ballet 2006; Helder et al. 2012). As a result, X-ray synchrotron emission originates from a much smaller volume than the radio synchrotron emission, which originates from the entire shell with lines of sight of $l \gtrsim 10^{18}$ cm. The shorter pathlengths probed in X-ray synchrotron radiation should result in less depolarization caused by variations in magnetic-field orientations along the line of sight. In addition, due to the steepness of the X-ray synchrotron spectrum, the intrinsic, maximum polarization degree could be larger than in the radio (Ginzburg & Syrovatskii 1965; Bykov et al. 2009).

However, as already stated above, the electron energies of 10–100 TeV necessary for X-ray synchrotron radiation require DSA in the presence of very turbulent magnetic fields immediately upstream of the shock fronts. Although shock compression enhances the tangential components of the magnetic field, a high level of magnetic-field turbulence may persist in the downstream region, perhaps even isotropizing the magnetic field due to non-linear interactions of the fluctuations downstream of the shock (Bykov et al. 2020). But it is also possible that the turbulence rapidly decays within the region producing the X-ray synchrotron radiation (Pohl et al. 2005). Whatever the mechanism that created the large scale radially oriented magnetic field inferred from radio emission is, this mechanism may already start to realign magnetic fields in a radial direction immediately downstream of the shocks (Jun & Norman 1996; Inoue et al. 2013). Note that an interesting feature of the X-ray synchrotron emission from Cas A is that it does not only arise from the forward shock, but also from the reverse shock region, in particular in the western part of the SNR (Helder & Vink 2008; Uchiyama & Aharonian 2008; Grefenstette et al. 2015), where the reverse shock appears to be moving toward the center instead of outward (Sato et al. 2018; Vink et al. 2022).

With the recent launch of the Imaging X-ray Polarimetry Explorer (IXPE) (Weisskopf et al. 2022), we can finally measure and map polarization with spatial resolution of a few tens of arcseconds. Cas A was the first science target of IXPE, and we report here the first detection of X-ray polarization from a shell-type SNR, albeit with a surprisingly low polarization degree of $\lesssim 4\%$. Although IXPE cannot resolve the X-ray synchrotron filaments, the fact that X-ray synchrotron radiation originates from within $\sim 10^{17}$ cm downstream of the shock, allows us to probe the magnetic-field orientation and isotropy to within this distance of the shocks.

In Section 2, we describe the measurements and analysis approach and the resulting polarization measurements. In Section 3 we discuss the implications of our results in the context of models for producing polarized emission from energetic particles in SNRs. Our conclusions are presented in Section 4. Details on the definition and treatment of the Stokes parameters, and on treatment of the unpolarized thermal emission in Cas A are given in Appendices.

2. OBSERVATIONS, DATA ANALYSIS AND RESULTS

IXPE is a NASA/ASI[1] small explorer (SMEX) mission that was launched on December 9, 2021. The polarization sensitive X-ray detectors are gas-pixel detectors (GPD) filled with dimethyl ether (Costa et al. 2001; Baldini et al. 2021), which are placed at the focus of three Wolter-1 mirror module assemblies giving telescopes with angular resolutions of 24″, 29″ and 30″ (half-power diameters) and each with a field of view of 12.9′ square (see Weisskopf et al. 2022; Soffitta et al. 2021). An X-ray photon interacting with the gas in the GPD results in the ejection of a photoelectron in the direction ϕ, which is distributed as $\cos^2\theta$, where θ is the polarization direction of the electromagnetic wave. The photoelectron ionizes the gas and produces secondary electrons, which form a charge cloud. These electrons, after drifting and mulitplication, are then detected and recorded by a finely pixellated detector plane. A moments analysis of the charge-cloud shape is used to reconstruct the initial photo-electron's direction, ϕ (see Bellazzini et al. 2003, for details).

The IXPE detectors are sensitive for polarization in the X-ray range from 2–8 keV, with a mirror effective area of 590 cm^2 at 4.5 keV for the three telescopes combined, reduced to a combined 26 cm^2 after accounting for detector quantum efficiency. The polarization sensitivity improves with energy, having a modulation factor of $\mu \sim 15\%$ at 2 keV to μ =50–60% at 8 keV. The modulation factor is the amplitude of the modulation due to polarization for a 100% polarized source in the absence of background. An ideal polarization detector will have $\mu = 100\%$. The detection of polarization also depends on the number of detected photons, which in turn depends on the source spectrum, the detector efficiency and the telescope effective area; for IXPE, the optimum energy for detecting polarization is roughly ~ 3 keV. Cas A's 2–8 keV spectrum is dominated by K-shell line emission from Si, S, Ar, Ca, and Fe, and continuum emission that is in many regions dominated by synchrotron radiation (e.g., Helder & Vink 2008, see also Appendix B). The 4–6 keV band has only weak line emission, but while using IXPE simulations based on imaging spectroscopy with the Chandra X-ray Observatory (Chandra for short) (Appendix B), we found that the 3–6 keV band offered a better sensitivity for detecting polarization, despite the presence of Ar-K and Ca-K line emission.

Cas A was the first science target of IXPE, after first observing the calibration source SMC X-1 during the one month commissioning phase. IXPE observed Cas A from January 11 to January 29, 2022, for a total time around 900 ks. We analyzed the data with the software package `ixpeobssim` (Baldini et al. 2022), which is used both for extraction of Stokes maps and spectra, as well as for Monte Carlo simulations. The analysis was based on processed high-level event list (level 2) in FITS format (see Rankin et al. 2022), which, apart from the usual columns for time, energy channel and sky and detector coordinates, also contains columns with $q_k \equiv 2\cos 2\phi_k$ and $u_k \equiv 2\sin 2\phi_k$, with ϕ_k the reconstructed photo-electron direction of event number k. This definition is different from Kislat et al. (2015) as the factor 2 is here part of the definition of q_k and u_k. Note that the values for q_k and u_k also contain a small correction, based on the method outlined by Rankin et al. (2022), which is necessary to remove the effects of a small modulation measured for an unpolarized source, as found and calibrated on ground. The stability of these corrections have been assessed on ground. For in-flight data the

---

[1] Agenzia Spaziale Italiana

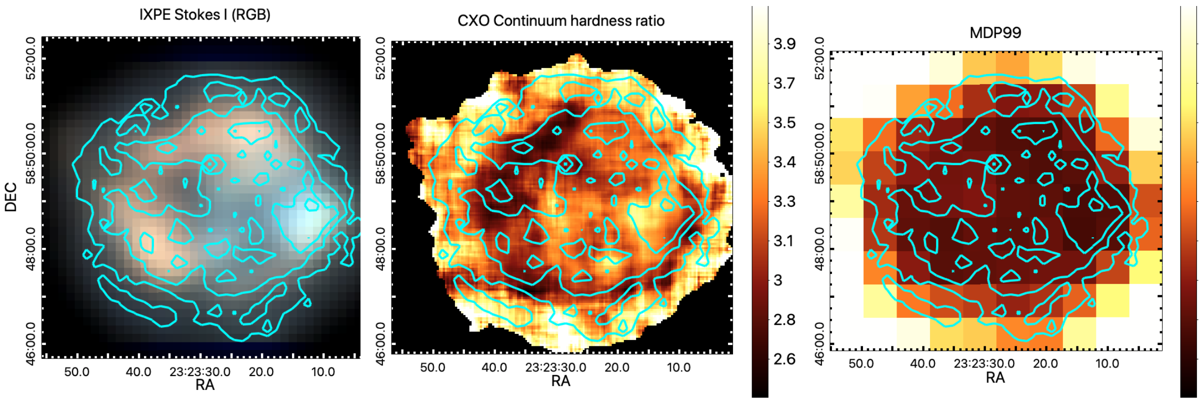

Figure 1. Left: IXPE three color Stokes I image with square-root brightness scaling, based on the 2–3 keV, 3–4 keV, and 4–6 keV bands, combined from the three detectors. The pixel size is $10.4''$ and the images have been smoothed with a gaussian kernel with $\sigma = 10.4''$. Center: Hardness ratio map based on Chandra X-ray data (ObsID 19606) using the 4.0–6.0 keV map divided by the 3.4–3.6 keV map, both dominated by continuum emission. The harder ratios ($\gtrsim 3$) likely correspond to synchrotron dominated continuum emission. Fluctuations due to differential absorption across the SNR are at the 9% level. Right: The MDP99 levels for the 3–6 keV band for the IXPE observations of Cas A. Here the map is binned to a pixel size of $42''$. In all panels we show the contours based on a recent 4–6 keV Chandra map using square-root brightness scaling (ObSID 19606).

stability of these corrections has not yet been assessed, but in the 3 to 6 keV band these effects are minor. We can therefore state that the results of our analysis are not affected by spurious modulation effects. For the present analysis, the values of q_k and u_k are based on the moment analysis of the charge clouds. In a future data release the determination of ϕ_k may be improved, once machine learning algorithms, currently under development (Peirson & Romani 2021), are employed.

During the early observations a number of calibration issues emerged and several corrections were applied. First of all, we filtered out likely particle background events using the electron tracks, as described by Xie et al. (2021) (see also Di Marco et al. in preparation). The fraction of the particle background removed was $\sim 30\%$, while less than 1% of the source was rejected. We found, however, the impact of the particle background on the polarization signal of Cas A to be negligible. Secondly, the reconstructed energies of the IXPE detected events in the level-2 data are known to have detector-dependent and time-dependent deviations, due to various effects, including charge built-up in the detectors. Throughout the whole observation the three detectors were calibrated during Earth occultations, by using onboard calibration sources, producing line emission at 1.7 keV (Si Kα) and 5.9 keV (^{55}Fe decaying into ^{55}Mn) (Ferrazzoli et al. 2020). Given the linearity of the response, the two energies allow for measuring both the slope and bias of the calibration. We reconstructed the time dependency of the channel-to-energy conversion. Thirdly, the boom connecting the X-ray telescopes with the spacecraft was affected by phase-dependent heating during its orbit around Earth. As a result the boom experienced time modulated bending, resulting in the focal point changing in detector coordinates. Corrections to these phase-dependent effects, some of which were also applied to the publicly released level 2 event list, still left an overall pointing reconstruction offset of the order of $2.5'$. In order to remove the offset we employed a spatial correlation code developed for measuring the expansion of Cas A (Vink et al. 2022), and used it to register the pointing solution of each detector unit to the 2019 (ObsID 19606) observation of Cas A with Chandra, for which we smoothed the Chandra image with $\sigma = 10.4''$. For this we used the 4-6 keV continuum band, as the morphology of Cas A in this band is relatively independent of the energy response of the detectors. This resulted in a pointing solution with an accuracy of about 1–$2''$. Finally, during the orbit, the pointing is affected by a switch between the two different star-trackers, one placed near the mirror module assemblies and viewing forward, and one placed on the spacecraft and looking in opposite direction. Currently this results in small periods of time with offsets in the pointing solutions. For the present analysis we filtered these short intervals out, leaving 819 ks of effective exposure time.

2.1. *Spatial exploration of polarization signals*

Maps of the Stokes parameters I, Q, and U are made with sums of u_k and q_k and a correction to account for the energy dependent modulation factor. See Appendix A for details. All maps shown are based on the summed maps of the three detector units. For the present analysis we did not use weights as we found that weighting with the modulation factor $w_k \propto \mu_k^{-2}$ (Vink &

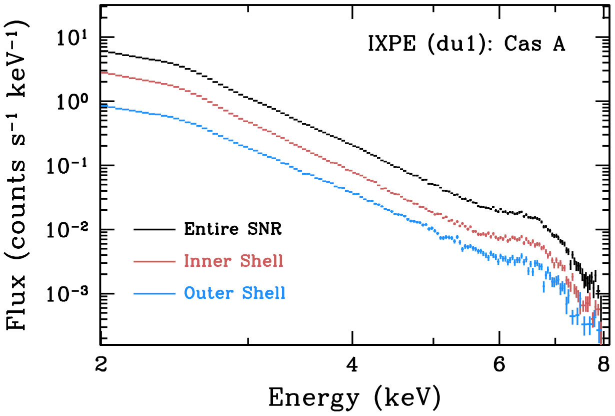

Figure 2. X-ray spectra of Cas A as detected by detector unit 1 of IXPE for three different extraction regions.

Zhou 2018) resulted only in minor to no improvements in the statistical significance.

In Fig. 1 we show the Stokes I three-band color map of Cas A with a pixel size of 10.4″, and the 3–6 keV map of the minimal detectable polarization at 99% confidence level (MDP99, see Appendix A) for a pixel size of 42″. The MDP99 map shows that polarization on these pixel scales can be detected at the $\sim 5\%$ polarization degree level in the interior regions, and up to 15% in the fainter outer regions. All maps also show the 4–6 keV contour lines based on Chandra observations, which serve as a point of reference for all derived polarization maps. Fig. 1 includes a hardness ratio map based on the 4-6 keV and 3.4–3.6 keV maps as observed by Chandra. The 3.4–3.6 keV band is also relatively devoid of line emission so this hardness ratio map shows which regions emit hard, and which regions emit soft X-ray continuum (c.f. Fig. 6 in Helder & Vink 2008). The hardness map illustrates in what regions X-ray synchrotron radiation is likely dominating the continuum emission: in the outer regions, and in some parts of the interior region—mostly the center, but with a prominent spot in the western interior region of Cas A. See also Appendix B. Although the energy resolution of IXPE is limited—with $\Delta E \approx 0.5$ keV at 2 keV and scaling inversely as the square root of the energy—one can still appreciate in the Stokes I map (Fig. 1, left) that the western part and outer regions have harder spectra (showing up bluish). The spectral capabilities can also be assessed from the detector 1 spectrum shown in Fig. 2 for three extraction regions. The Si-K and S-K line emission do not show up as broadened lines as is the case with CCD spectra, but rather lead to noticeable inflections around 3 keV (Si-K and S-K) and around 6 keV (caused by Fe-K emission). For the current paper we concentrated fully on the spatial analysis.

Analyzing the full Q and U maps we did not find any regions for which we can report a significant detection of a polarization signal. We did find regions with polarization signals above the 3σ pre-trial confidence level. However, given that the statistics depend on the pixel-size used, and also on the fact that Cas A is covered by about $\sim$200 angular resolution regions, we cannot confidently say that our analysis of the Q and U maps provide significant detections. For example, for 200 pixels the expected number of false positive detections at the 3σ level (99.73% confidence) is 0.5 pixel. The post-trial probability for a spurious detection at the the pre-trial 3σ level is 42% $(= 1 - (99.73\%)^{200})$.

Nevertheless, the $\sim 3.5\sigma$ signals do deserve to be mentioned, first because future, improved data analysis or additional data may be able to confirm these signals as solid detections, and secondly because these polarization "hotspots" illustrate the low level of X-ray polarization degree of Cas A on small scales.

In Fig. 3 we show two maps of polarization significance (using a χ^2_2-map) and the polarization degree for a pixel sizes of 42″ and 84″. For the polarization degree map we only show the pixels with detection confidence above 99.73% confidence level. The most significant signal has $\chi^2_2 = 15.9$, corresponding to a 3.57σ confidence level. The hotspots correspond to polarization degrees ranging from 3.4% (inner region, using 84″ pixels) to 19% (outer, forward shock region, using 42″ pixels). These values are just above the MDP99 level. In the future, with an improved analysis chain, we may be able to lower the MDP99 level and increase sensitivity to regions with lower degrees of polarization.

2.2. *Analysis based on an assumed circular magnetic-field topology*

The pixel-by-pixel polarization measurement yielded tentative detections of polarization with polarization degrees of 4%–15% at the 3σ–4σ confidence level, too low to claim a solid detection. Binning into larger pixel sizes improves the polarization statistics, but at the expense of potential depolarization due to the mixing of regions with different polarization angles. However, given the roughly spherical symmetry of Cas A itself, as well as the long-known radial symmetry of the magnetic-field orientation as inferred from radio observations, one can improve the statistics by summing over large regions by assuming a circular symmetry to the polarization direction. Although the radio polarization measurements suggest an a priori radial magnetic-field orientation, shock compression of a highly turbulent mag-

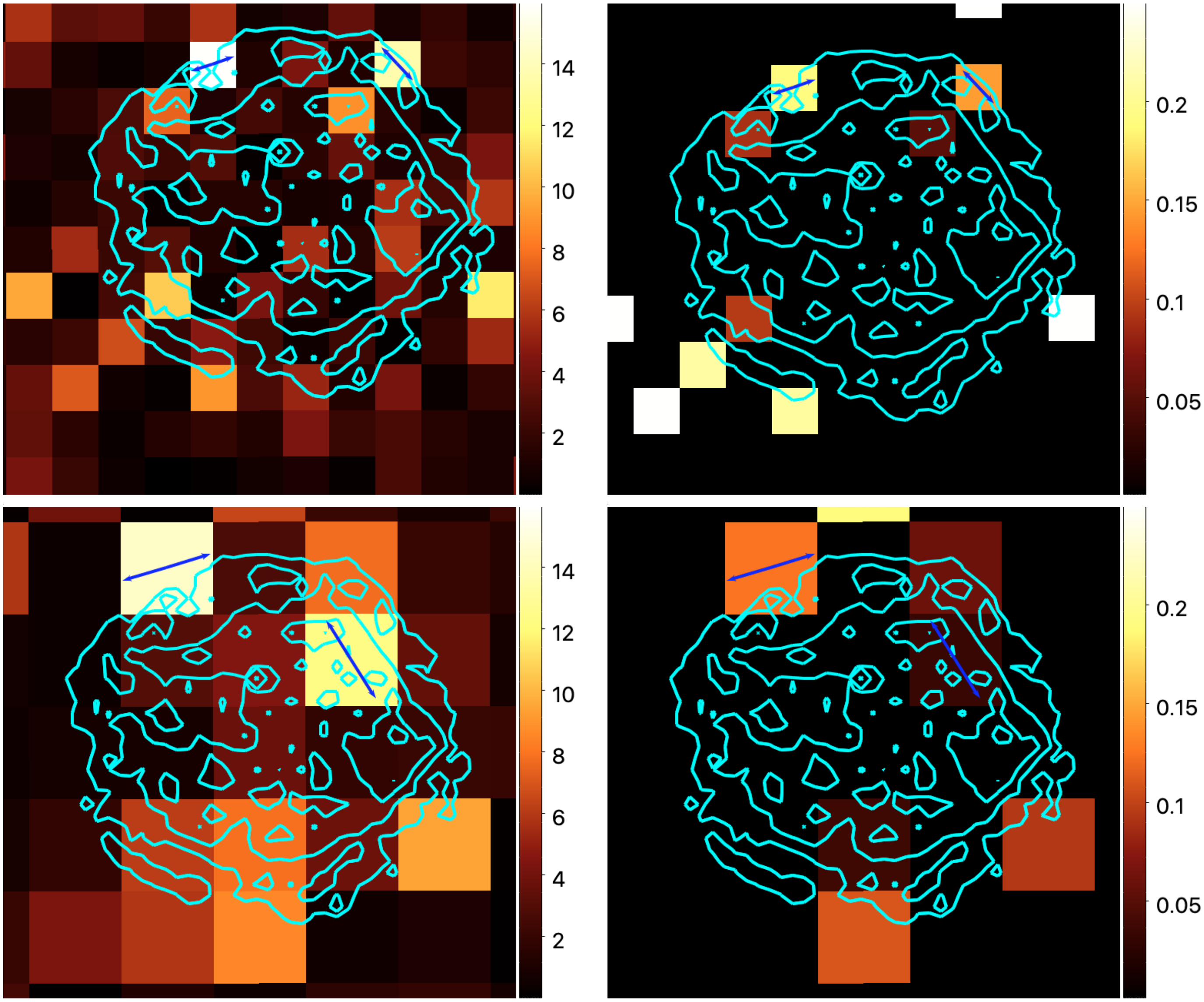

Figure 3. Left: Maps of χ_2^2 (or $S_{i,j}$, see Appendix A) values for the polarization signal for the 3-6 keV band. Right: the corresponding polarization degree maps. Only pixels with pre-trial confidence levels above 2σ ($\chi_2^2 > 6.28$) are shown. For pixels with $\chi_2^2 > 11.8$ (corresponding to 3σ confidence level) the polarization angles are indicated with blue arrows. The errors on these angles are $\sim 8^\circ$. Top row: maps with pixel sizes binned to $42''$. Peaks in the χ_2^2 map are $\chi_2^2 = 15.9, 13.6$ corresponding to polarization degrees of 19%, and 14.5%. Bottom row: same plot, but with a larger pixel size of $84''$. Peaks in the χ_2^2 map are $\chi_2^2 = 14.4, 12.3$ corresponding to polarization degrees of 12.4% and 3.4%.

netic field instead would lead to an enhancement of the tangential component (e.g. Jun & Norman 1996; Bykov et al. 2020). Note that the polarization direction for synchrotron radiation is perpendicular to the magnetic-field orientation: a tangential polarization signal corresponds to a radial magnetic field, and vice versa.

Assuming a circular symmetry for the polarization direction, we recalculated the q_k and u_k values for each event, by calculating a new zero for the direction of the photo-electron (ϕ) based on the sky coordinate, and its position angle with respect to the center of Cas A, for which we used the explosion center determined by Thorstensen et al. (2001). This procedure results in new values q'_k and u'_k, which can be summed over large regions to provide an overall signal corresponding to the radial and tangential Stokes parameters Q' and Stokes U'.

In Fig. 4 we show the chosen annuli for which we obtained Q' and U'. They cover the central region, the reverse shock regions (overlapping with the bright shell), and the outer region, which contains the synchrotron filaments associated with the forward shock. Since the

Table 1. Polarization measurements in annuli and western region after imposing circular symmetry for Stokes U and Q.[a]

	$R_{\rm min}$ [b] (arscec)	$R_{\rm max}$ (arcsec)	MDP99 (%)	Pol. Degree (%)	PD Corrected [c] (%)	Angle [d] (°)	Significance
Central region (CR)	0	65	2.4	< 3.1	< 4.0	N/A	0.9σ
Reverse shock (RS)	65	140	1.3	1.6 ± 0.4	1.9 ± 0.5	77.2 ± 7.6	3.1σ
RS West (RSW) [e]	65	140	2.6	< 3.9	< 4.6	N/A	1.9σ
Forward shock (FS)	140	216	2.3	3.5 ± 0.7	4.8 ± 1.0	89.8 ± 6.1	4.1σ
FS + RSW [f]	216	216	1.7	3.0 ± 0.6	3.6 ± 0.7	87.2 ± 5.4	4.8σ
All	0	216	1.0	1.8 ± 0.3	2.4 ± 0.4	85.7 ± 5.2	4.9σ

[a] See main text for an explanation. Listed errors correspond to 1σ (68% confidence) ranges.

[b] The central coordinate used was $\mathrm{RA}_{J2000} = 23^{\rm h}23^{\rm m}27.8^{\rm s}$, $\mathrm{DEC}_{J2000} = 58°48'49.4''$, which is the explosion center determined by Thorstensen et al. (2001).

[c] The inferred polarization degree for the synchrotron component only, see Appendix B

[d] An angle of 90° corresponds to tangential polarization vector associated with a radial magnetic field orientation.

[e] This region is a subset of the "Reverse shock" region.

[f] This combines the Reverse shock West and Forward shock region.

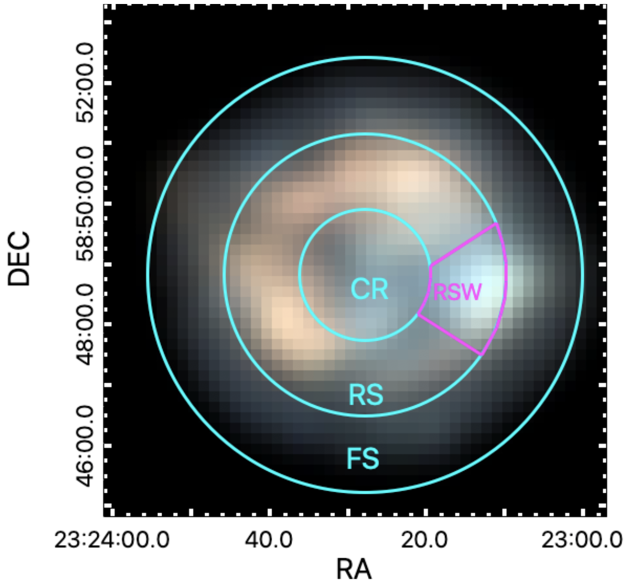

Figure 4. IXPE map, similar to Fig. 1, with superimposed the regions that were used to test for an overall radial or tangential polarization vector orientation. See Table 1.

western reverse shock region shows evidence for strong X-ray synchrotron emission (e.g., see Helder & Vink 2008; Grefenstette et al. 2015, and also the bluish part in the multiband Stokes I image in Fig. 1), we also isolate just the western part of the reverse shock region.

The resulting polarization measurements are listed in Table 1. Apart from the polarization degree we list under "PD Corrected" the inferred polarization degree of the synchrotron component only. For these we used the spectral parameter maps based on Chandra observations; see Appendix B.

The errors listed should be used with caution, since polarization degree and polarization angle are not independent statistical quantities, both being derived from a combination of Q' and U'. A better representation of the measurements is obtained by graphically representing the Stokes Q' and U' parameters in a polar diagram, with confidence contours. These are plotted in Fig. 5, which shows that for the "forward shock region" and the "forward shock + western region" the 1σ confidence contour is outside the MDP99 region (in pink). For the "forward shock region" the polarization detection significance is over 4σ pre-trial, corresponding to a roughly 3σ post-trial confidence level, while for the "forward shock + west region" and all data combined the detection is close to a 5σ pre-trial confidence level, corresponding to a better than 4σ post-trial confidence level. Note that the underlying statistics are not Gaussian, so the quoted σ values are for ease of interpretation, whereas the diagrams show the full confidence areas in the polarization-degree versus polarization-angle plane. For the most significant detections we find that the polarization angle is consistent with a tangential polarization pattern, corresponding to a radial magnetic-field orientation.

3. DISCUSSION

The IXPE observations of Cas A reveal that the polarization level is low at the spatial resolution of IXPE ($\sim 30''$), with a tangentially oriented polarization component with a polarization degree of $\approx 1.5 \sim 3.5\%$,

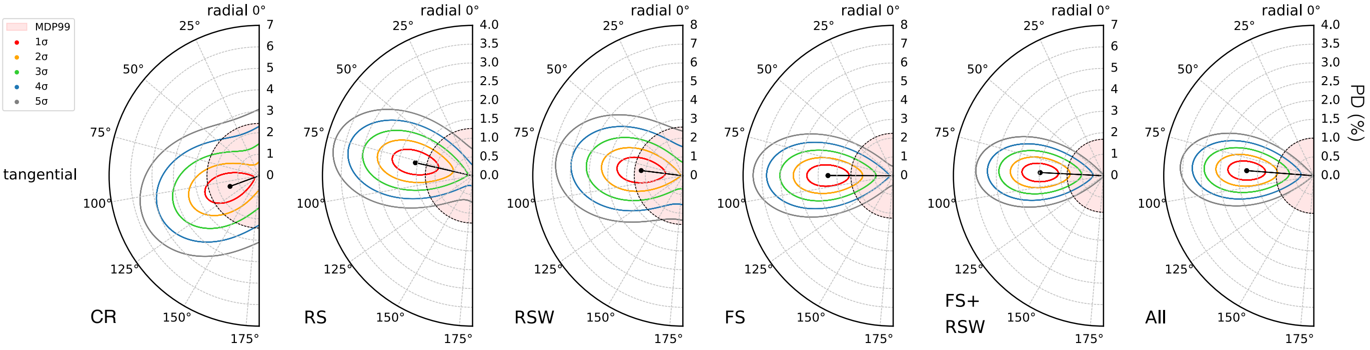

Figure 5. Polar diagrams depicting the measured polarization degree and angle with respect to circular symmetry as confidence contours for the six regions listed in Table 1. The radial coordinate indicates the polarization degree in percent. The pink region corresponds to the MDP99 level. Values around 90° correspond to an overal tangentially oriented polarization averaged over the region, while around 0° indicates on average a radially oriented polarization.

corresponding to $\approx$ 2.5 to $\sim$ 5% for the synchrotron component only. The polarization signal is associated with the X-ray synchrotron bright features in Cas A: the outside region associated with the forward shock, and the western part of the reverse shock region (see Vink & Laming 2003; Helder & Vink 2008; Uchiyama & Aharonian 2008; Grefenstette et al. 2015, for maps of the X-ray synchrotron radiation). The detection of the weak polarization signal requires the assumption of circular symmetry, but even without this assumption the polarization degree cannot be much larger than 4% for the interior (reverse shock) of Cas A, and 15% at the outer boundary, as indicated by the MDP99 levels, and the tentative indications of polarization for individual regions with angular extents of $\sim$42″–84″. High degrees of polarization may be present for unresolved regions and they need to have more or less random polarization directions.

The low polarization degree and the tangential polarization pattern are compatible to what has been measured in the radio band (e.g. Rosenberg 1970; Braun et al. 1987; Anderson et al. 1995). Nevertheless, these X-ray polarization results still come as a surprise. First of all, in X-rays the synchrotron spectrum has steepened, leading to higher intrinsic polarization degrees (Ginzburg & Syrovatskij 1967; Bykov et al. 2009). Secondly, X-ray synchrotron radiation in Cas A originates from a narrow region of $\lesssim 10^{17}$ cm immediately downstream of the shocks, which reduces depolarization caused by the line of sight crossing regions with different polarization angles. And thirdly, at the shock front the perpendicular (tangential) component of the magnetic field is compressed, so close to the shock front a radial instead of a tangential polarization angle is expected.

Apart from line of sight effects, a low polarization degree may indicate a turbulent magnetic field, in particular for angular scales smaller than the IXPE angular resolution. The level of magnetic-field turbulence near the shock regions in Cas A is expected to be high, as a high level of turbulence is required for accelerating electrons to $\gtrsim$ 10 TeV — the energy needed for producing X-ray synchrotron radiation. However, efficient DSA assumes a high magnetic-field turbulence in the unshocked plasma, whereas the shock compression should enhance the tangential component of the magnetic field.

Simulations of X-ray polarization signals to be expected for young SNRs by IXPE by Bykov et al. (2020) predicted polarization degrees of 30%–70%, assuming an anisotropic magnetic field—i.e. with a preferred orientation due to shock compression—and with a turbulence spectrum cutting off at 10^{18} cm, which is compatible with the IXPE angular resolution. For isotropic magnetic fields the polarization degree predicted by Bykov et al. (2020) is similar to the values reported here: $\sim 5\% - 15\%$. Based on these models the magnetic-field turbulence near the shock may be close to isotropic, perhaps due to nonlinear interactions of the fluctuations downstream from the shock, as hypothesised by Bykov et al. (2020). In addition, it may also indicate that the magnetic-field turbulence wavelength cutoff is well below 10^{18} cm.

An alternative reason for the low degree of polarization may be that the synchrotron emission is coming from a mix of plasma with the expected tangential oriented magnetic field immediately downstream of the shock, and a more radially oriented magnetic field further downstream of the shock, but still within 10^{17} cm of the shock.

Although a radial magnetic-field orientation throughout the SNR has been inferred from radio observations, its origin has never been fully understood. There are two main hypotheses: (i) there are magnetohydrodynamical (MHD) process stretching the magnetic fields, and (ii) the radial magnetic field is the result of a selection effect, related to efficient acceleration wherever the magnetic-field orientation at the shock happens to be quasi-parallel.

As for hypothesis (i), it was long suspected that the radially oriented magnetic fields are caused by filamentation due hydrodynamical instabilities, such as Rayleigh-Taylor instabilities at the contact discontinuity between shocked ejecta and shocked circumstellar plasma (Gull 1973). MHD simulations confirm the formation of a radially oriented magnetic field near the contact discontinuity, but the regions near the forward shock are predicted to have a tangential magnetic field Jun & Norman (1996). Inoue et al. (2013) performed MHD simulations of the shock front in the presence of a clumpy medium, resulting in Richtmeyer-Meshkov instabilities which reorient the overall magnetic-field orientation from a tangential to a radial direction within a distance of $\sim 7 \times 10^{17}$ cm from the shock. This length scale is almost an order of magnitude larger than the width of the X-ray synchrotron filaments, but the MHD length scale is dependent on initial conditions, such as the size and density contrasts of the clumps. Very Large Array (VLA) radio polarization measurements by Gotthelf et al. (2001) lend some support to this hypothesis, as they report a swing in polarization angle near the forward shock. However, the radio polarization measurements were based on an azimuthal integration over 55°, resulting in an effective spatial resolution that is larger than the widths of the X-ray filaments.

Regarding hypothesis (ii), West et al. (2017) investigated what the impact is if DSA preferentially occurs wherever the shock has a quasi-parallel magnetic-field orientation (i.e., a significant component parallel to the shock velocity vector), motivated by the likely magnetic-field orientation in SN 1006 (Rothenflug et al. 2004). As the plasma is advected downstream and keeps roughly its magnetic-field orientation, the synchrotron radiation becomes biased toward radial magnetic fields. The likely reason for efficient electron acceleration at quasi-parallel shocks probably concerns the initial injection of low energy electrons into the acceleration process. If the observational selection bias still pertains to X-ray synchrotron radiation, the implication is that the responsible $\gtrsim 10$ TeV electrons should not have diffused too far away from the original regions with preferentially radial magnetic fields. This would imply that the shock regions with quasi-parallel magnetic fields are associated with a characteristic turbulence wavelength, λ_B, that must be comparable in size to the diffusion length scale ($l_{\rm diff}$). For $l_{\rm diff} \ll \lambda_B$ one expects a strong polarization signature, whereas for $l_{\rm diff} \gg \lambda_B$ the selection effect hypothesis by West et al. (2017) should not pertain to X-ray synchrotron radiation. The relevant diffusion length scale is that for the tangential diffusion component, which should be $l_{\rm diff} \approx \sqrt{D\tau_{\rm loss}} \approx 3 \times 10^{16} \eta^{1/2} (B/250\ \mu{\rm G})^{-1/2}$ cm, with the diffusion coefficient given by $D = \frac{1}{3}\eta cE/(eB)$, where $\eta \geq 1$ is the ratio between the mean-free path of the particles and their gyroradius (see Introduction for the other definitions). The length scale of 3×10^{16} cm corresponds to $0.6''$, which is comparable to the Chandra point spread function. Since the X-ray synchrotron filaments as seen by Chandra appear to be smooth, hypothesis (ii) requires the diffusion length scale to be smaller than 3×10^{16} cm, requiring $\eta \sim 1$ and $B > 250\ \mu$G.

So although the IXPE observations do not favor one hypothesis for the radial magnetic-field orientation over the other, the measured polarization signal puts constraints on relevant length scales. For the hypothesis that an MHD process leads to radial magnetic fields, the IXPE results require that the reorientation happens within 10^{17} cm downstream of the shock. In contrast, the hypothesis that the radial magnetic field orientation is caused by a selection effect sets constraints on the wavelength of the magnetic-field turbulence of $\lambda_B \lesssim 3 \times 10^{16}$ cm.

4. CONCLUSIONS

We reported here on the very first detection of X-ray polarization from a shell-type SNR—the young and bright core-collapse SNR Cas A, which was the first science target of the NASA IXPE mission. We employed two different methods to measure the polarization signals: a pixel-by-pixel analysis, and a more sensitive analysis that assumes a circular symmetry for the polarization vectors, and then summing over large regions.

The pixel-by-pixel analysis provides tentative hints of polarization in the 3–6 keV band at the 3σ to 4σ pre-trial confidence level, with associated polarization degrees ranging from 3% to 19%, just above the local minimum detectable polarization degree at 99% confidence (MDP99). Taking into account post-trial factors these detections are not significant. The analysis assuming circular symmetry for the polarization angles provides solid detections (close to 5σ) for an annular regions encompassing the forward shock region, and a region covering the entire SNR. The corresponding polarization degrees are lower than the polarization generally reported in the radio: 1.8–3.5% in X-rays versus $\sim 5\%$ in the radio band (e.g., see Rosenberg 1970, for radio polarization measurements with a resolution comparable to IXPE). Even after correction for the contribution of thermal X-ray emission in the 3-6 keV band, this suggests an X-ray synchrotron polarization degree of 2.4–4.8%, which is similar, or slightly lower than in the radio band. Like in the radio band, the polarization vectors suggest an overall radial magnetic-field orientation.

Since the X-ray synchrotron radiation is confined to regions within $\lesssim 10^{17}$ cm, the IXPE results imply that the radial magnetic-field structure is already present close to the shock. This is surprising since shock compression imposes an overall tangential magnetic-field orientation immediately downstream of the shock. If the long-known overall radial magnetic-field structure is due to hydrodynamical instabilities radially stretching the magnetic field (Jun & Norman 1996; Inoue et al. 2013), the IXPE results imply that this process reorients the magnetic field from tangential to radial within $\lesssim 10^{17}$ cm downstream of the shock. On the other hand, if the radial magnetic-field alignment is a selection effect related to more efficient acceleration in those shock regions where there is a quasi-parallel field (West et al. 2017), then the high energy of the X-ray synchrotron emitting electrons suggests that quasi-parallel shock acceleration takes place over length scales similar to the tangential electron diffusion length scale of $\sim 3 \times 10^{16}$ cm.

The measured low polarization degree is consistent with a nearly isotropic magnetic-field turbulence as simulated by Bykov et al. (2020). But this would require a mechanism of increasing the magnetic-field turbulence downstream of the shock, so perhaps it is more likely that the low polarization degree is due to a mix of tangential and radial magnetic fields, either due realignments within the X-ray synchrotron filaments, or due to electron diffusion washing out the selection effect.

The Imaging X ray Polarimetry Explorer (IXPE) is a joint US and Italian mission. The US contribution is supported by the National Aeronautics and Space Administration (NASA) and led and managed by its Marshall Space Flight Center (MSFC), with industry partner Ball Aerospace (contract NNM15AA18C). The Italian contribution is supported by the Italian Space Agency (Agenzia Spaziale Italiana, ASI) through contract ASI-OHBI-2017-12-I.0, agreements ASI-INAF-2017-12-H0 and ASI-INFN-2017.13-H0, and its Space Science Data Center (SSDC), and by the Istituto Nazionale di Astrofisica (INAF) and the Istituto Nazionale di Fisica Nucleare (INFN) in Italy. This research used data products provided by the IXPE Team (MSFC, SSDC, INAF, and INFN) and distributed with additional software tools by the High-Energy Astrophysics Science Archive Research Center (HEASARC), at NASA Goddard Space Flight Center (GSFC). J.V. & D.P. are supported by funding from the European Union's Horizon 2020 research and innovation program under grant agreement No. 101004131 (SHARP). The research at Boston University was supported in part by National Science Foundation grant AST-2108622. We thank Dawoon Kim for kindly providing us with his script for making polar plots of polarization degree and angle.

Facilities: IXPE

Software: `ixpeobsim` (Baldini et al. 2022)

REFERENCES

Anderson, M. C., Keohane, J. W., & Rudnick, L. 1995, ApJ, 441, 300, doi: 10.1086/175356

Arnaud, K. A. 1996, Astronomical Society of the Pacific Conference Series, Vol. 101, XSPEC: The First Ten Years, ed. G. H. Jacoby & J. Barnes, 17

Baldini, L., Bucciantini, N., Di Lalla, N., et al. 2022, arXiv e-prints, arXiv:2203.06384. https://arxiv.org/abs/2203.06384

Baldini, L., Barbanera, M., Bellazzini, R., et al. 2021, Astroparticle Physics, 133, 102628, doi: 10.1016/j.astropartphys.2021.102628

Ballet, J. 2006, Advances in Space Research, 37, 1902, doi: 10.1016/j.asr.2005.03.047

Bamba, A., Yamazaki, R., Yoshida, T., Terasawa, T., & Koyama, K. 2005, ApJ, 621, 793, doi: 10.1086/427620

Bellazzini, R., Angelini, F., Baldini, L., et al. 2003, in Society of Photo-Optical Instrumentation Engineers (SPIE) Conference Series, Vol. 4843, Polarimetry in Astronomy, ed. S. Fineschi, 383–393, doi: 10.1117/12.459381

Borkowski, K. J., Lyerly, W. J., & Reynolds, S. P. 2001, ApJ, 548, 820, doi: 10.1086/319011

Braun, R., Gull, S. F., & Perley, R. A. 1987, Nature, 327, 395, doi: 10.1038/327395a0

Bykov, A. M., Uvarov, Y. A., Bloemen, J. B. G. M., den Herder, J. W., & Kaastra, J. S. 2009, MNRAS, 399, 1119, doi: 10.1111/j.1365-2966.2009.15348.x

Bykov, A. M., Uvarov, Y. A., Slane, P., & Ellison, D. C. 2020, ApJ, 899, 142, doi: 10.3847/1538-4357/aba960

Costa, E., Soffitta, P., Bellazzini, R., et al. 2001, Nature, 411, 662

Di Marco, A., Costa, E., Muleri, F., et al. 2022, AJ, 163, 170, doi: 10.3847/1538-3881/ac51c9

Dickel, J. R., & Jones, E. M. 1990, in IAU Symposium, Vol. 140, Galactic and Intergalactic Magnetic Fields, ed. R. Beck, R. Wielebinski, & P. P. Kronberg, 81

Dickel, J. R., & Milne, D. K. 1976, Australian Journal of Physics, 29, 435

Ferrazzoli, R., Muleri, F., Lefevre, C., Morbidini, A., & Amici, F. o. 2020, Journal of Astronomical Telescopes, Instruments, and Systems, 6, 048002, doi: 10.1117/1.JATIS.6.4.048002

Flett, A. M., & Henderson, C. 1979, MNRAS, 189, 867, doi: 10.1093/mnras/189.4.867

Funk, S. 2017, High-Energy Gamma Rays from Supernova Remnants, ed. A. W. Alsabti & P. Murdin, 1737, doi: 10.1007/978-3-319-21846-5_12

Ginzburg, V. L., & Syrovatskii, S. I. 1965, ARA&A, 3, 297, doi: 10.1146/annurev.aa.03.090165.001501

Ginzburg, V. L., & Syrovatskij, S. I. 1967, in IAU Symposium, Vol. 31, Radio Astronomy and the Galactic System, ed. H. van Woerden, 411–+

Gotthelf, E. V., Koralesky, B., Rudnick, L., et al. 2001, ApJL, 552, L39, doi: 10.1086/320250

Greco, E., Vink, J., Miceli, M., et al. 2020, A&A, 638, A101, doi: 10.1051/0004-6361/202038092

Grefenstette, B. W., Reynolds, S. P., Harrison, F. A., et al. 2015, ApJ, 802, 15, doi: 10.1088/0004-637X/802/1/15

Gull, S. F. 1973, MNRAS, 161, 47, doi: 10.1093/mnras/161.1.47

Helder, E. A., & Vink, J. 2008, ApJ, 686, 1094, doi: 10.1086/591242

Helder, E. A., Vink, J., Bykov, A. M., et al. 2012, SSRv, 173, 369, doi: 10.1007/s11214-012-9919-8

Hughes, J. P., Rakowski, C. E., Burrows, D. N., & Slane, P. O. 2000, ApJL, 528, L109.

Hwang, U., & Laming, J. M. 2012, ApJ, 746, 130, doi: 10.1088/0004-637X/746/2/130

Hwang, U., et al. 2004, ApJL, 615, L117, doi: 10.1086/426186

Inoue, T., Shimoda, J., Ohira, Y., & Yamazaki, R. 2013, ApJL, 772, L20, doi: 10.1088/2041-8205/772/2/L20

Jones, T. J., Rudnick, L., DeLaney, T., & Bowden, J. 2003, ApJ, in press

Jun, B.-I., & Norman, M. L. 1996, ApJ, 472, 245, doi: 10.1086/178059

Kenney, J. D., & Dent, W. A. 1985, ApJ, 298, 644, doi: 10.1086/163648

Kislat, F., Clark, B., Beilicke, M., & Krawczynski, H. 2015, Astroparticle Physics, 68, 45

Koyama, K., et al. 1995, Nature, 378, 255

Laming, J. M., & Hwang, U. 2003, ApJ, 597, 347

Malkov, M. A., & Drury, L. 2001, Reports of Progress in Physics, 64, 429

Marshall, H. L. 2021, AJ, 162, 134, doi: 10.3847/1538-3881/ac173d

Mayer, C. H., & Hollinger, J. P. 1968, ApJ, 151, 53, doi: 10.1086/149418

Patnaude, D. J., & Fesen, R. A. 2009, ApJ, 697, 535, doi: 10.1088/0004-637X/697/1/535

Peirson, A. L., & Romani, R. W. 2021, ApJ, 920, 40, doi: 10.3847/1538-4357/ac157d

Pohl, M., Yan, H., & Lazarian, A. 2005, ApJL, 626, L101, doi: 10.1086/431902

Rankin, J., Muleri, F., Tennant, A. F., et al. 2022, AJ, 163, 39, doi: 10.3847/1538-3881/ac397f

Reed, J. E., Hester, J. J., Fabian, A. C., & Winkler, P. F. 1995, ApJ, 440, 706.

Rosenberg, I. 1970, MNRAS, 151, 109, doi: 10.1093/mnras/151.1.109

Rothenflug, R., et al. 2004, A&A, 425, 121.

Sato, T., Katsuda, S., Morii, M., et al. 2018, ApJ, 853, 46, doi: 10.3847/1538-4357/aaa021

Shklovsky, J. S. 1954, in Liege International Astrophysical Colloquia, Vol. 5, Liege International Astrophysical Colloquia, 515

Soffitta, P., Baldini, L., Bellazzini, R., et al. 2021, AJ, 162, 208, doi: 10.3847/1538-3881/ac19b0

Sun, X. H., Reich, P., Reich, W., et al. 2011, A&A, 536, A83, doi: 10.1051/0004-6361/201117693

Thorstensen, J. R., Fesen, R. A., & van den Bergh, S. 2001, AJ, 122, 297

Uchiyama, Y., & Aharonian, F. A. 2008, ApJL, 677, L105, doi: 10.1086/588190

Vink, J., & Laming, J. M. 2003, ApJ, 584, 758.

Vink, J., Patnaude, D. J., & Castro, D. 2022, ApJ, 929, 57, doi: 10.3847/1538-4357/ac590f

Vink, J., & Zhou, P. 2018, Galaxies, 6, 46, doi: 10.3390/galaxies6020046

Völk, H. J., Berezhko, E. G., & Ksenofontov, L. T. 2005, A&A, 433, 229

Weisskopf, M., Soffitta, P., Baldini, L., et al. 2022, Journal of Astronomical Telescopes, Instruments, and Systems, 8, 1 , doi: 10.1117/1.JATIS.8.2.026002

West, J. L., Jaffe, T., Ferrand, G., Safi-Harb, S., & Gaensler, B. M. 2017, ApJL, 849, L22, doi: 10.3847/2041-8213/aa94c4

Wilms, J., Allen, A., & McCray, R. 2000, ApJ, 542, 914, doi: 10.1086/317016

Xie, F., Ferrazzoli, R., Soffitta, P., et al. 2021, Astroparticle Physics, 128, 102566, doi: 10.1016/j.astropartphys.2021.102566

Zirakashvili, V. N., & Ptuskin, V. S. 2008, ApJ, 678, 939, doi: 10.1086/529580

APPENDIX

A. CALCULATION OF THE Q AND U MAPS

The polarization of radiation as measured by IXPE is calculated based on the reconstructed ejection angle of the photo-electron, ϕ_k, associated with event k. Maps of the Stokes parameters I, Q and U can then be obtained using (weighted) sums of $q_k = 2\cos 2\phi_k$ and $u_k = 2\sin 2\phi_k$, which can also include the correction for the energy- or event-dependent modulation factor μ_k:

$$\begin{aligned} I_{i,j} =& W_{i,j}^{-1}\sum_k \frac{w_{k,i,j}}{\mu_k}, \\ Q_{i,j} =& W_{i,j}^{-1}\sum_k \frac{w_{k,i,j}q_{k,i,j}}{\mu_k}, \\ U_{i,j} =& W_{i,j}^{-1}\sum_k \frac{w_{k,i,j}u_{k,i,j}}{\mu_k}, \end{aligned} \tag{A1}$$

with $W_{i,j} \equiv \sum_k w_{k,i,j}$ the sum of the weights. This definition of Stokes I is chosen so that the polarization fraction can be expressed as $\Pi_{i,j} = \sqrt{Q_{i,j}^2 + U_{i,j}^2}/I_{i,j}$. Note that the division by μ_k ensures that the detector response to polarization, which is energy dependent, is taken into account.

The weights w_k can be based on the quality of the reconstruction of ϕ_k (Marshall 2021; Di Marco et al. 2022), or on the energy dependent modulation factor (Vink & Zhou 2018), $w_k = \mu_k^{-2}$, or simply ignored, i.e. $w_k = 1$. The variances in the Stokes parameters are

$$\begin{aligned} \mathrm{Var}(I_{i,j}) =& W_{i,j}^{-2}\sum_k \frac{w_{k,i,j}^2}{\mu_k^2}, \\ \mathrm{Var}(Q_{i,j}) =& W_{i,j}^{-2}\sum_k \frac{w_{k,i,j}^2 q_{k,i,j}^2}{\mu_k^2}, \\ \mathrm{Var}(U_{i,j}) =& W_{i,j}^{-2}\sum_k \frac{w_{k,i,j}^2 u_{k,i,j}^2}{\mu_k^2}. \end{aligned} \tag{A2}$$

The polarization detection significance can be obtained by the methods described in e.g. Kislat et al. (2015); Vink & Zhou (2018), but we note here that in the absence of polarization the expectation values for the Stokes parameters are $E[Q] = 0$ and $E[U] = 0$, and that $\cos 2\phi$ and $\sin 2\phi$ are orthogonal functions. As a result the statistical quantity

$$S_{i,j} \equiv \frac{Q_{i,j}^2}{\mathrm{Var}(Q_{i,j})} + \frac{U_{i,j}^2}{\mathrm{Var}(U_{i,j})} \tag{A3}$$

has a χ^2 distribution with two degrees of freedom. One can make a map of $S_{i,j}$, which we call a χ^2 map, that shows how consistent the observed polarization signal is with the null hypothesis (i.e., no polarization signal) in pixel (i, j). A large value of $S_{i,j}/\chi^2_{2,i,j}$ indicates, therefore, the presence of a polarization signal for pixel i, j with a confidence corresponding to χ^2_2. A 3σ signal corresponds to $\chi^2_2 = 11.8$, 4σ to $\chi^2_2 = 19.3$, and 5σ to $\chi^2_2 = 28.7$.

In the absence of an intrinsic polarization signal the expectation values for the variances are $E[\mathrm{Var}(Q_{i,j})] = E[\mathrm{Var}(U_{i,j})] = 2W_{i,j}^{-2}\sum_k(w_{k,i,j}^2/\mu_k^2)$, since $E[(u^2 + q^2)] = 4$. Assuming that $\mathrm{Var}(Q_{i,j}) \approx \mathrm{Var}(U_{i,j})$, we can express the polarization degree as

$$\Pi_{i,j} = \sqrt{\frac{Q_{i,j}^2 + U_{i,j}^2}{I_{i,j}^2}} = \sqrt{\frac{S_{i,j}\,\mathrm{Var}(Q_{i,j})}{I_{i,j}^2}}. \tag{A4}$$

By noting that $S_{i,j}$ is χ^2_2 distributed and that the 99% confidence range corresponds to $\chi^2_2 = 9.21$ we see that the minimal detectable polarization (MPD$_{99}$) degree is

$$\mathrm{MDP}_{99} = \sqrt{\frac{9.21 \times 2W_{i,j}^2\sum_k(w_{k,i,j}^2/\mu_k^2)}{W_{i,j}^{-2}\sum_k(w_{k,i,j}^2/\mu_k)^2}} = \frac{4.29}{\sqrt{\sum_k(w_{k,i,j}^2/\mu_k)}}, \tag{A5}$$

equivalent to the expression derived by Kislat et al. (2015). The extraction of Stokes parameters over larger regions, after a local rotation of q_k and u_k, follows the same procedure as outlined here, except that the final outcome should not have a pixel index (i, j), but a region label.

Note that summing together $S_{i,j}$ over various pixels, by for example rebinning ($S_{i',j'} = \sum_{i,j} S_{i,j}$), results in yet another χ^2 distribution, but now with more degrees of freedom. For example, rebinning $S_{i,j}$ by 2×2 pixels, results in χ^2_8 distribution. Essentially this is an incoherent addition of the signal, so less sensitive than rebinning $Q_{i,j}, U_{i,j}$ (i.e. coherent summing), but it has the advantage that it is not sensitive to rotations of the polarization vector within the binned pixels region.

B. ASSESSING THE NONTHERMAL CONTRIBUTION ACROSS CAS A

The radio emission from Cas A is almost exclusively caused by synchrotron radiation, but the emission in the 0.5-10 keV consists of a mixture of thermal radiation (line emission, bremsstrahlung, free-bound and two-photon emission) and synchrotron radiation.

At the resolution of the Chandra X-ray observatory, the synchrotron emission stands morphogically apart (Hughes et al. 2000; Vink & Laming 2003; Hwang et al. 2004), being confined to narrow filaments, which may nevertheless also determine the continuum in projection toward the rest of the SNR. The thermal emission from Cas A is dominated by emission from shocked ejecta (Laming & Hwang 2003). In order to prepare for the IXPE observations of Cas A, but also to estimate the contribution of the synchrotron radiation to each IXPE pixel as a function of energy, we modeled the emission from Cas A based on fitting Chandra X-ray spectra from the whole of Cas A, divided in tiles of $20''$ by $20''$. We used for the modeling the *xspec* package version 12.12 (Arnaud 1996), and concentrated on a single, 164 ks Chandra observation (ObsID 4638) (Hwang et al. 2004).

The best-fit model per individual tiles were then folded through the spatial and spectral response functions of IXPE using the *ixpeobsim* instrumental response functions. For IXPE simulations we imposed a polarization degree and orientation on the X-ray synchrotron component. Before the launch of IXPE we used these simulations to test and optimize the analysis tools used for the results presented in this paper, but at the final stage, after indeed obtaining detections, we also used the simulations to translate the measured polarization degree into a polarization degree for just the synchrotron component. The simulations also indicated that the 3–6 keV band provided a more sensitive band for detecting polarization than the 4–6 keV (nearly) line-free band, as the broader band considerably improves the statistics.

The model consists of three thermal components, for which we used the *vnei* model (Borkowski et al. 2001), a power-law component to fit the synchrotron contribution, and the Galactic absorption model, *tbabs* (Wilms et al. 2000, which was also used for the abundances). The power-law slope was constrained to be $\Gamma = 2.8$–3.4, i.e., within $\Delta\Gamma = 0.3$ of the average spectral index for the synchrotron component of $\Gamma = 3.1$ measured by Helder & Vink (2008). The three *vnei* components represented the metal-dominated ejecta, with the components representing oxygen-, silicon-, and iron-rich plasma. The abundances of these elements were set to 10,000 in order to simulate almost pure metal plasmas, which also enhances the contributions of free-bound and two-photon continuum (Greco et al. 2020). The oxygen-rich plasma was also responsible for the neon- and magnesium-line emission, and the silicon-rich plasma for the intermediate mass elements, but with the abundances of these elements as free parameters. Additional free parameters were the temperatures, constrained to 0.4–4 keV (4.5 keV for Fe); ionization ages ($n_e t$, constrained between 2×10^9–8×10^{11} cm^{-3}s); the Galactic absorption column ($N_{\rm H}$); the normalizations of the emission components; and Doppler shifts for the silicon- and iron-rich components.

Examples of maps with the best-fit parameters of these models are shown in Fig. 6.[2] We do not claim that these are best-possible models for the emission of Cas A, as it is based on an automated procedure, sometimes manually assisted for particularly bad fits. But the final models fit the Chandra spectra generally well. This can be judged from the example spectral fits in Fig. 6, one of which includes the worst fit in terms of the C-statistic. In general we find that the centroid of the Fe-K line emission is not well fitted. This centroid is determined by the plasma temperature, ionization age and Doppler shift. However, the ionization age and temperature also determine the iron L-shell emission between 0.8-1.4 keV, and cannot be arbitrarily varied. So a likely cause of the centroid mismatch is that the Fe-L and Fe-K emission may arise from various plasma components, suggesting that one plasma component for Fe-rich ejecta is not sufficient. The Galactic absorption map and the ionization age of the Si-rich component compare well with the

---

[2] We will archive the complete model files at https://zenodo.org, which will also include all data products used for this paper.

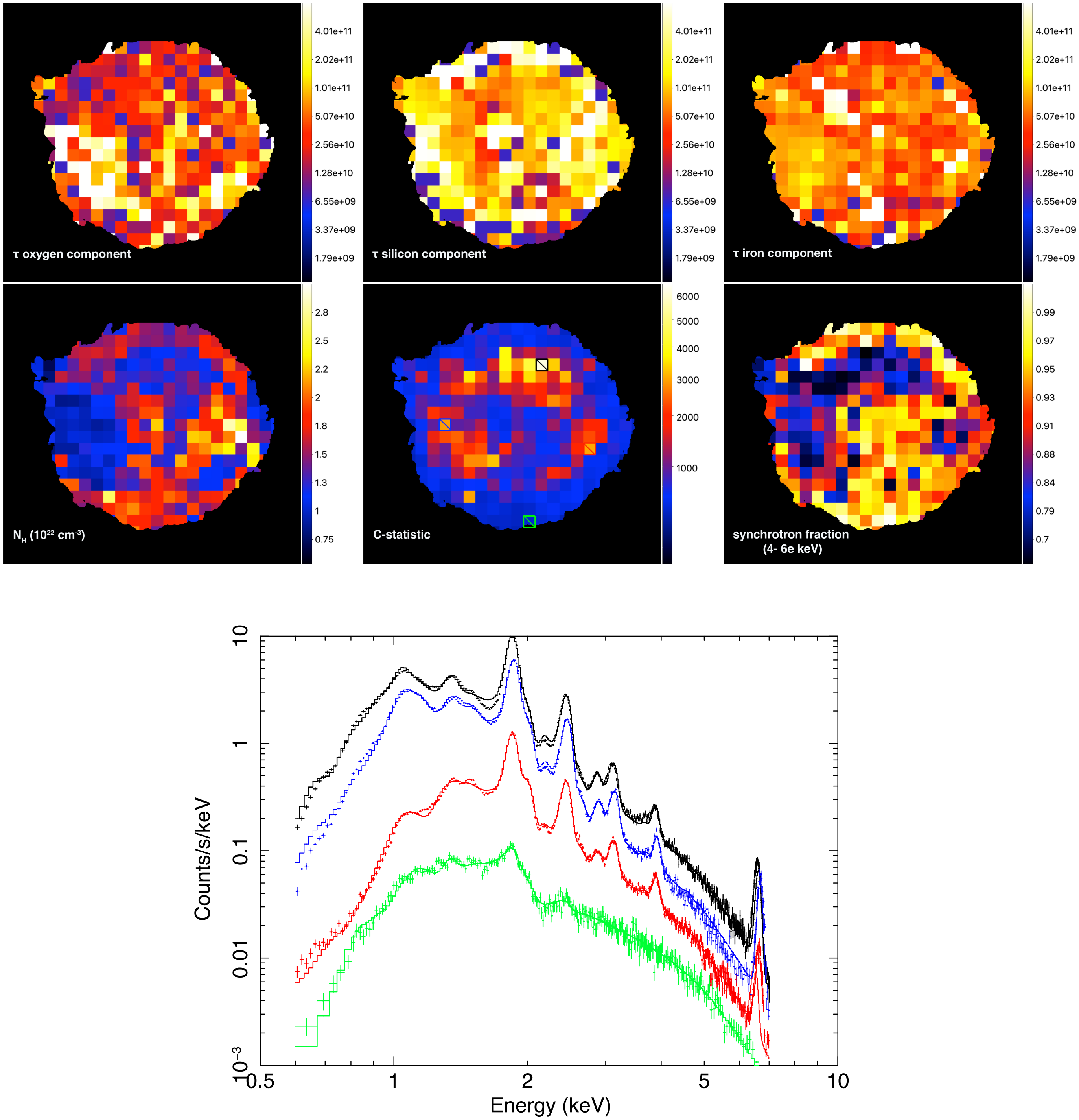

Figure 6. Examples of the maps of relevant parameters created from the output automated fitting of Chandra X-ray observations (ObsID 4638). We used these maps, and similar ones, to generate simulated IXPE event lists for assessing polarization degrees of the synchrotron components as a function of position and energy band. The top row shows the $\tau = n_e t$ values in units of cm^{-3}s for the oxygen-rich, silicon-rich (i.e. rich in intermediate mass elements), and iron-rich plasma components, respectively. The second row shows the absorption map ($N_{\rm H}$ in cm^{-2}), the C-statistic values of the best fits, and the fraction of synchrotron radiation with respect to the overall flux in the 4–6 keV band. Finally, the bottom panel shows four spectra obtained by the fitting routine. The colors correspond to those of the crossed squares in the C-statistic map. The fits are generally satisfactory, but the iron line centroids appear off in the top three spectra.

ones provided in Hwang & Laming (2012). However, we note that Hwang & Laming (2012) did not include a full fitting of the nonthermal component in their analysis.

The values from the synchrotron continuum fraction were used to correct the observed polarization degree to the corresponding value for the synchrotron component. A perhaps surprising by-product of the Chandra spectral mapping is that we find that fits indicate that the contribution of the synchrotron radiation to the overall continuum emission is surprisingly high, ranging from 38% to nearly 100%. Helder & Vink (2008) already showed that this might be the case based on the extrapolation of the hard X-ray continuum measured by BeppoSAX-PDS to the 4-6 keV band (their Fig. 5), but estimated a more conservative 54% overall contribution. Nevertheless, the map of the synchrotron continuum fraction in Fig. 6 matches well morphologically with Fig. 6 (right) in Helder & Vink (2008) and the NuStar 10–15 keV map in Fig. 6 (right) in Grefenstette et al. (2015).